Depletion of Electroactive Species in Microchannels. Theory and Experimental Validations for Quantitative Abatement of Interfering Species under Stagnant Conditions

Catherine Sella, Laurent Thouin

Depletion of Electroactive Species in Microchannels. Theory and Experimental Validations for Quantitative Abatement of Interfering Species under Stagnant Conditions.

Catherine Sella and Laurent Thouin*

PASTEUR, Département de chimie, Ecole normale supérieure, PSL University, Sorbonne Université, CNRS, 75005, Paris, France

*** Corresponding author:** laurent.thouin@ens.psl.eu

Abstract. The generation of an electroactive-species depleted microenvironment was investigated by taking advantage of confinement in microchannels under stagnant conditions. High depletion rates can be achieved with paired microband electrodes but the time scale of experiment must be carefully delimited based on device geometry, electrochemical cell configuration and species diffusivity. Numerical simulations were thus carried out to reach the situation of interest when the diffusion coupling and lateral diffusion in the microchannel becomes predominant with the operation of the electrodes. The optimal conditions for two minimal cell configurations (*i.e.*, with two or three working electrodes) were delineated by establishing a zone diagram. Experimental validations were successfully performed (i) to illustrate the depletion rate achieved between two side electrodes, and (ii) to demonstrate the selective detection of a target analyte in presence of interfering species by using three electrodes. These situations can easily be extrapolated to the case of regular microelectrode arrays within microchannels.

Keywords: confinement ; microchannel ; microelectrode ; amperometry ; diffusion coupling.

1. Introduction

Due to the development of manufacturing techniques based on micro and nanotechnologies, electrode arrays have received increased attention for emerging new miniaturized electrode devices and novel applications in chemical sensing and biosensing [1-4]. In particular, recent advances are driven by the development of smart sensors and wearable devices in various fields including environmental and healthcare monitoring [5]. In systems where electrodes are individually addressable, electrodes can operate either as single entities or paired electrodes [6]. These systems give the opportunity of sensing simultaneously numerous analytes with high spatio-temporal resolution. One the one hand, they benefit from the well-known properties of single microelectrodes (small size, high current density, fast time response, reduced IR drop, steady-state …) [7-10]. On the other hand, with overlap of diffusion layers, closely spaced electrodes provide interesting properties of dual-electrode systems [11,12]. One is the possibility to monitor electrogenerated intermediates with short lifetimes for revealing reaction mechanisms [13-16]. Another is to enhance the currents by redox cycling of reversible species for improving the sensitivity of electrochemical responses. Similar to a rotating ring-disc electrode, the performance is governed by the collection efficiency which depends on the geometry and degree of miniaturization of the electrochemical cells. Indeed, a large variety of microsystems were suggested including double and triple-microband assemblies [17-20], microchannel electrodes [21-23], thin-layer cells [24-26], recessed electrodes [16,27,28], and interdigitated electrodes [6,14,27,29-31].

As for many electrochemical sensors, selectivity is a crucial issue to be addressed as well as sensitivity. In this context, redox cycling between electrodes allows species to be distinguished by their electron transfer kinetics according to the diffusion time scale imposed by the interelectrode distance. As no redox cycling occurs with irreversible species, a strategy is to differentiate chemically reversible species from irreversible electroactive interferents. This has been largely developed in scanning electrochemical microscopy (SECM) [32] or with interdigitated electrodes [33]. Another strategy to achieve selective detection is based on redox cycling and interferent depleting with systems adopting the configuration of plane-recessed electrodes [34-37]. By holding a proper potential to the plane electrode, an interferent-depleted microenvironment is created at the recessed electrode, blocking access of interfering species to cavities. By maintaining the redox cycling of analytes, this detection strategy enhances sensitivity

further and breaks limitation of the reversible-irreversible systems mentioned above. Note that a potential difference should exist between the target analyte and interfering species. Interestingly, if the plan electrode is left floating (*i.e.*, not connected with the potentiostat), the device still exhibits redox cycling since the electrode acts as a bipolar electrode [38]. Actually, this bipolar mode [39,40] is similar to the positive feedback mode encountered in SECM [41].

To deplete interfering species, an innovative strategy has been developed in microfluidic systems where successive operations can be performed under flow conditions along a microchannel [42-45]. The redox cycling between electrodes is eliminated but a depletion step can be implemented upstream with the operation of a so-called depletion electrode: by applying an appropriate potential, the interfering species are selectively electrolyzed before the target analyte reaches downstream the electrode where it is only detected. In previous studies, we demonstrated, theoretically and experimentally, that complete removal of interfering species is achieved if a thin-layer regime [46,47] is established at the depletion electrode [44,48,49]. The aim of this work is to extend the depletion performance within a microchannel under stagnant solution conditions. Indeed, a flow requires a larger volume of samples to be processed than in stopped-flow mode where the volumes can be only a few picoliters to nanoliters depending on the dimensions of the device. Moreover, compared to the other strategies mentioned above that operate in open solutions, the space is more restricted, which necessarily results in a higher confinement effect. The objective is therefore to integrate two side microband electrodes polarized at the same potential to generate maximum depletion of electroactive species in the interelectrode space. Theoretically, whatever the device geometry, 100% depletion rate must be achieved at long times by bulk electrolysis. However, to reach such a level, the time scale of experiment must be carefully targeted according to the device geometry, electrochemical cell configuration and diffusivity of species. In the following, mass transport in the vicinity of paired electrodes was studied theoretically under stopped-flow condition. To delineate the diffusion regimes that are established between the electrodes, a minimal and simple configuration with two working electrodes (2WE) was first considered (Fig. 1A). A wide range of conditions was investigated by numerical simulations depending on the device geometry and time scale of experiment. Next, a three-working-electrode configuration (3WE) was considered with the aim of integrating a concentration probe electrode at mid-distance (Fig. 5A) to (i) electrochemically assess the

depletion rate in the interelectrode space and (ii) to detect a target analyte in presence of interfering species. In both 2WE and 3WE minimal configurations, experiments were conducted in a microchannel to validate the theoretical predictions. $Fe(CN)_6^{4-}$ was used as the model redox species. An equimolar mixture of hydrogen peroxide H_2O_2 and nitrite NO_2^- was also tested in order to illustrate in this case the selective detection of a target analyte (here NO_2^-) in presence of interfering species (H_2O_2).

2. Experimental

2.1. Materials and solutions

Phosphate buffered-saline solutions (PBS; pH 7.4; 0.140 M NaCl, 0.01 M Na_2HPO_4, 2.68 mM KCl) were prepared by dissolving tablets (Sigma) in deionized water (Milli-Q, Millipore Corporation). 2 mM solutions of potassium ferrocyanide $Fe(CN)_6^{4-}$ (Acros organics) were then prepared in PBS. Under these conditions, the diffusion coefficient of $Fe(CN)_6^{4-}$ was estimated equal to $D_{FeII} = 6\ 10^{-6}$ cm^2 s^{-1} [50] whereas the diffusion coefficient ratio between $Fe(CN)_6^{4-}$ and $Fe(CN)_6^{3-}$ was taken equal to $D_{FeII}/D_{FeIII} = 0.85$ [51]. Before experiments with the mixture of hydrogen peroxide H_2O_2 and nitrite NO_2^-, 2 mM H_2O_2 solutions (from 35wt %, Acros) and 2 mM H_2O_2 of nitrite NO_2^- (from 99.99% $NaNO_2$, Aldrich) were freshly prepared in PBS from stock solutions respectively. The diffusion coefficients of H_2O_2 and NO_2^- were taken equal to $1.5\ 10^{-5}$ cm^2 s^{-1}.

2.2. Microdevices

The fabrication of the microfluidic device was reported elsewhere [50]. The device is made of two parts assembled together. The top part was a block of polydimethylsiloxane (PDMS), on which a linear channel (1.5 cm length, 800 µm width) with two reservoirs at each end (0.3 cm diameter) were engraved on one block side. The height of both the microchannel and reservoir was h = 20 µm. The bottom part was a glass substrate on which several parallel platinum microband electrodes (Ti/Pt with 5 nm/20 nm thickness) were patterned by metal deposition and soft lithography. After assembling the two parts, the electrodes were positioned perpendicular to the microchannel. The effective length of the microband electrodes was thus delimited by the microchannel width. Two sets of working electrodes and one counter electrode (CE) were thus positioned along the microchannel (Fig. S1A). The reference electrode

(RE) was a Ag/AgCl wire dipped aside in one of the two reservoirs. To maintain a good sealing between the glass substrate and the PDMS block, the CE was composed of three short-circuited microbands of 200 µm width, separated by a gap of 40 µm. Each set of working electrodes included a central microband WE_c (30 µm width) surrounded by two side microbands WE_s (50 µm width). Depending on the set of working electrodes, the gap distance *g*' between the electrodes was either 50 µm or 100 µm. Note that only one set was connected during the experiments. All the characteristic dimensions of the microdevice were reported in Fig. S1B. The volume of solution needed to fill the microchannel including the inlet and outlet reservoirs was approximately a hundred of nanoliters.

2.3. Electrochemical experiments

All electrochemical experiments were performed at room temperature by using a multipotentiostat (Autolab type PGSTAT128N, Eco Chemie) with Nova 2.1.3 software. The working electrodes were biased independently and their responses were monitored individually. Two operating modes were defined for each 2WE and 3WE configuration. In the 2WE configuration, the single and dual modes corresponded respectively to the cases where a single WEs or the pair of WEs was connected. In the 3WE configuration, the modes ON and OFF corresponded respectively to the cases where the pair of WEs was connected or not during the operation of WEc. In chronoamperometry with $Fe(CN)_6^{4-}$ solution, all the electrodes were biased at +0.4 V/RE on the oxidation plateau of $Fe(CN)_6^{4-}$. With the mixture of H_2O_2 and NO_2^-, the pair of WE_s was biased at +0.5 V/RE on the oxidation plateau of H_2O_2 while WEc was biased at +0.85 V/RE on the oxidation plateau of NO_2^-. To ensure control of the electrochemical processes by mass transport and to avoid inhibitory effects on nitrite oxidation due to the possible formation at pH 7.4 of oxide layers on the electrode surface, the working electrodes were previously activated by performing 5 cycles between -1V and 0.8V at 0.7 Vs^{-1} scan rate followed by 5 cycles between 0.1V and 1V at 0.5 Vs^{-1} in PBS solution before each measurement [52].

2.4. Numerical simulations

Numerical simulations of chronoamperometric responses based on the 2WE and 3WE configurations were performed by using the Electrochemistry module of COMSOL Multiphysics 6.0 software. To

encompass a maximum of experimental conditions including a variety of microdevices geometries, dimensionless parameters were defined and introduced for computation (see below).

3. Theory for a dual-electrode configuration

The formulation of the problem was simplified by only considering the operation of two working electrodes WE_s in a microchannel without flow (Fig. 1A). In this approach, the boundary diffusion regimes and the associated electrode responses were evaluated in chronoamperometry as a function of device geometry and time scale.

3.1. Formulation of the problem

The configuration was a dual electrode assembly with two identical and parallel microband electrodes of width *w* and length *l*, located on the floor of a rectangular microchannel, and separated by a gap distance *g*. In the case under investigation, the width of the microchannel was equal to the length *l* of the microbands. Since *l* was much larger than *w*, the problem could be reduced to the formulation of a problem in 2D space (Fig. 1B). Dimensionless parameters were introduced to generalize the solutions with the following:

- coordinates $X = x/h$ and $Y = y/h$,
- size parameters $W = w/h$ and $G = g/h$
- and time scale $\tau = Dt/h^2$.

Note that h^2/D is the characteristic time for diffusion to extend vertically across the channel with *D* the diffusion coefficient.

A reversible one-electron electrochemical reaction was considered:

$$A + e^- \rightleftharpoons B \qquad (1)$$

where A is the reactant at initial concentration c^0 and B the product.

For simulations performed in chronoamperometry under diffusion control, only the mass transport equation for species A was taken into account:

$$\frac{\partial C}{\partial \tau} = \left(\frac{\partial^2 C}{\partial X^2} + \frac{\partial^2 C}{\partial Y^2} \right) \qquad (2)$$

with $C = c / c^0$.

Concentration profiles of A within the microchannel were thus numerically evaluated by solving Eq. (2) by finite elements according to:

- the initial condition within the entire microchannel $\tau = 0, C = 1$
- the condition at insulating boundaries $\tau \geq 0, \partial C/\partial Y = 0$
- the condition at both electrode surfaces $\tau \geq 0, C = 0$.

According to the symmetry of the system, both working electrodes have the same dimensionless current Ψ defined by:

$$\Psi(\tau) = \frac{i(t)}{\mathrm{F}lDc^\circ} = \int_0^W \left(\frac{\partial C(\tau)}{\partial Y} \right)_{Y=0} \mathrm{d}X \qquad (3)$$

where i is the current and F the Faraday.

3.2. Boundary diffusion regimes

Fig. 1C shows some concentration profiles simulated in chronoamperometry at a dual electrode assembly. Different situations may be reached depending on the geometry and time scale of experiment. In other words, diffusion length is the key parameter controlling different operating regimes and transitions between them. Therefore, successive steps may be briefly described as the following. (i) At sufficiently short time, diffusion at both electrodes is planar. (ii) When diffusion layer becomes larger than the electrode width, hemicylindrical diffusion develops, provided that the channel height remains high enough [53]. Indeed, when the channel height imposes a physical limitation, diffusion becomes planar lateral with diffusion layer expanding along the microchannel walls for each individual microband [50,54]. (iii) When diffusion length exceeds the gap distance between electrodes, both diffusion layers overlap. In this case, depletion / electrolysis of species starts between the electrodes. Concomitantly, the phenomenon is emphasized when diffusion length exceeds the microchannel height. Under such conditions, confinement effects are maximal and full depletion can be achieved between the electrodes. A steady-state regime is locally established while diffusion continues to spread laterally at each outer edges of the electrodes.

Since diffusion length is time related, the regime of interest can be systematically reached at long times whatever the configuration of dual electrodes considered. However, the time scale for which experimental conditions are fulfilled depends on the geometry of the microdevice (microchannel height, gap between electrodes, electrode size) and to less extend on the diffusion coefficient.

3.3. Cottrellian-type current responses

From a theoretical point of view, apart from the concentration profiles simulated above, limiting currents can be already deduced for the different diffusion regimes. Corresponding equations of limiting currents are reported in Table 1. Indeed, as can easily be deduced, planar (P) and planar lateral (PL) regimes exhibit the well-known "Cottrellian-type" behavior [50]. They differ from each other by the surface area controlling the current. In planar diffusion, the surface area is that of the electrode. In planar lateral diffusion, the surface area is twice the channel cross section since limiting diffusion takes place on either side of the electrode. In this case, the current no longer depends on the electrode size but on the microchannel dimensions. Accordingly, the novel regime described above leading to maximum depletion between electrodes will display the same type of behavior. Since full depletion is achieved on one side of the electrode, diffusion only occurs on the opposite side. Compared to PL regime, diffusion is still planar lateral but the surface area controlling the current is divided twice and equal to the channel cross section. In the following, this new regime leading to maximum confinement will be called PLc (*see* Table 1).

As a function of time, current responses of the electrodes must successively follow a given sequence of diffusion regimes imposed by the device geometry. Apart from given transitions occurring between these regimes, currents always decay as the square root of time. At first sight, it is difficult to distinguish the regime of interest PLc from others, namely when the depletion takes place between the two electrodes. The objective was thus to delimit the optimal conditions based on simulations and characteristics given above.

Regime	Current	Dimensionless current	Eq.
P	$i^{\mathrm{P}} = \frac{\mathrm{F}Ac^{\circ}\sqrt{D}}{\sqrt{\pi t}}$ with $A = wl$	$\Psi^{\mathrm{P}} = \frac{W}{\sqrt{\pi\tau}}$	(4)
PL	$i^{\mathrm{PL}} = \frac{\mathrm{F}Ac^{\circ}\sqrt{D}}{\sqrt{\pi t}}$ with $A = 2hl$	$\Psi^{\mathrm{PL}} = \frac{2}{\sqrt{\pi\tau}}$	(5)
PLc	$i^{\mathrm{PLc}} = \frac{\mathrm{F}Ac^{\circ}\sqrt{D}}{\sqrt{\pi t}}$ with $A = hl$	$\Psi^{\mathrm{PLc}} = \frac{1}{\sqrt{\pi\tau}}$	(6)

Table 1: Equations of current in chronoamperometry for planar diffusion (regime P), planar lateral diffusion on both sides of electrode (regime PL), and planar lateral diffusion on a single side of electrode (regime PLc). *A* is the surface area controlling the regime.

4. Results and discussion

4.1. Zone diagram for a dual-electrode configuration

In order to span a large range of experimental conditions and to delineate the limiting regimes foreseen above, simulations were performed in chronoamperometry over a time range up to five orders of magnitude. In a first attempt, results were analyzed for $W = 2$ and for increasing values G from 0.1 to 50 (Fig. 2A). As expected, when G is high enough, no diffusion coupling occurs between the electrodes. This is better observed on a logarithmic plot of same data in Fig. 2B. In such a case, each electrode behaves as individual electrodes : planar diffusion initiates at short times (regime P, Eq. (4)) followed by planar lateral diffusion (regime PL, Eq. (5)) at longer times. In the particular case when $W = 2$, Eqs. (4) and (5) turn out to be identical, meaning that no transition can be clearly observed as a function of time when $\tau > 100$ and $G > 50$. For lower G values, diffusion coupling can take place between electrodes. Under those conditions, the current deviates clearly from initial regime P or PL towards the new planar lateral regime PLc (Eq. (6)). This situation is encountered the faster the smaller the gap. Before reaching PLc, a transition regime is established, characterized by a very sharp decrease of current over a short period of time (Fig. 2B). It corresponds to the particular case where the diffusion layer thickness is constrained by the microchannel walls with moderate lateral propagation along the

microchannel (regime TL, Fig. 1C). Note that no relationship of current can be deduced for this transition.

In order to delineate the geometry and time scale conditions leading to the prevalence of each regime, assessments were made on the basis of the following criterion:

$$\frac{\Psi_{\text{ref}} - \Psi}{\Psi_{\text{ref}}} = 0.1 \qquad (7)$$

where Ψ_{ref} is the dimensionless current of a reference diffusion regime (P, PL or PLc).

A zone diagram (G,τ) was thus established from previous data by applying Eq. (7) in combination with Eqs. (4)-(6). Three main areas were thus defined showing the occurrence of individual P, PL and PLc regimes versus G and τ (Fig. 2C). The conditions under which diffusion layer between electrodes start to interact were also outlined by plotting on the zone diagram the corresponding boundary (dashed line in Fig. 2C). It was derived from Eq. (7) by taking Ψ_{ref} as the current simulated for a single-electrode configuration (*i.e.*, only one electrode within the microchannel). Accordingly, PLc regime is located on the right side of this boundary where diffusion coupling between electrodes prevails. PLc regime is achieved following two distinct situations. Indeed, when $G < 1$, a single transition from P to PLc regimes takes place. In this case, PLc regime is reached for $\tau > 1$, whatever G. When $G > 1$, two transitions arise successively, *i.e.*, from P to PL and then from PL to PLc. In this case, conditions to reach PLc regime depend both on τ and G.

Since the electrode size W is supposed to have no influence on the diffusion coupling between electrodes, it was checked that these properties were still observed for other W values (*i.e.*, W = 0.1, 1, 10 and 5). Fig. 2D displays a zoom of the upper part of the diagram where the transition from PL to PLc regimes is observed. Data show that this transition does not depend on W (see symbols in Fig. 2D) but it is only controlled by the time required for individual diffusion layers to overlap. In a first approximation, the boundary of the PLc area varies linearly with time whatever W. Considering the time scale τ / G^2 (*i.e.*, Dt/g^2), conditions for PLc regime to be established can be rationalized as follows:

$$G > 4 \text{ and } \tau > (G/1.58)^2 \qquad (8)$$

4.2. Depletion rate between two electrodes

To assess the influence of depletion in the interelectrode space under the PLc regime, the local concentrations were evaluated at mid-distance between the electrodes, either on the floor or the ceiling of the microchannel (Fig. 3A). Data are plotted in Fig. 3B as a function of time with simulated concentrations for $W = 2$ and G ranging from 1 to 50. As expected, c/c^0 decreases with τ leading to similar concentration variations exhibiting a rapid and high decay. Moreover, as soon as $G > 2$, concentration variations on the floor and on the ceiling become identical, indicating under these conditions that a perfectly homogeneous concentration is established over the channel height. At longer times, all concentrations tend to zero, which highlights the drastic influence of confinement as well as the depletion achieved between the electrodes. Additional simulations show that the boundary of PLc regime established previously in Fig. 2B corresponds approximately to a concentration level of $c/c^0 = 0.03$ (Fig. S2). An example of the curves in Fig. 3B is plotted in Fig. 3C (*i.e.*, curve a with $G = 2$) using a logarithmic scale, while the corresponding concentration profiles are displayed in Fig. 3D at various selected times. Both figures show that after the sharp decrease, the concentrations reach lower levels with a more moderate variation. In comparison with the previously established regimes, the sharp decrease of current clearly occurs during the TL transition while the lowest concentrations are reached in the PLc regime. Note that when $G > 100$, only a slight decrease in concentration is observed (curve b, Fig. 3C).

In order to accurately estimate the concentrations reached in the PLc regime, simulated data were analyzed using a logarithmic concentration scale for different G and W values (Fig. 4). For comparison, prevalence areas of the PLc regime were also delimited with grey areas. Fig. 4A displays some of the data of Fig. 3B simulated for $W = 2$. The curves show that once the PLc regime is established, concentrations follow exactly the same trend, whatever G. Conversely, in Fig. 4B are plotted data for $G = 2$ and several W values. In this case, as deduced from Fig. 2C, the PLc regime is achieved at a given time whatever W, immediately after the sharp decrease in concentration. However, the levels of concentration attained under these conditions depend strongly on W. Indeed, concentration can be lowered by five orders of magnitude by only increasing W by a factor of 5. An interesting property is that for a given W, concentration varies with the square root of time such as:

$$\frac{c}{c^0} = \frac{k_W}{\sqrt{\pi\tau}} \quad (9)$$

where k_w is a constant depending on W. Values of k_w were estimated from Fig. 4B and plotted in Fig. 4C as a function of W. An empirical, but simple relationship, was then derived with:

$$\log k_W = -0.15 - 0.69W \quad (10)$$

Therefore, the assessment of residual concentrations between the electrodes can be easily performed without any simulations by first considering the time condition (Eq. (8)) required for the PLc regime to be established, and then using Eqs. (9)-(10). From an experimental point of view, the comparison between current variations and Eq. (6) gives also an additional information in order to check if optimal conditions are fulfilled experimentally for a complete depletion.

4.3. Implementation of a third electrode

The incorporation of a third electrode WEc in the mid-gap between the two electrodes WEs was then considered for a three-working-electrode (3WE) configuration (Fig. 5A). Note that this configuration corresponds to the situation when electrochemical measurements can be performed by this electrode at the location within the microchannel where depletion is established. As mentioned in introduction, when considering the application where interfering species are abated for detecting selectively a given species, the potential of WEc is necessarily different (higher for oxidation processes and lower for reduction processes) than that of WEs. Nevertheless, whatever the case envisioned, WEc contributes by its own operation (both with the two WEs) to the depletion rate, in particular when all the electrodes WEs and WEc are biased simultaneously. In such a situation, the time required for depletion to be achieved should be shorter depending on the size W_c of this electrode. Simulations were then carried out based on a 3WE configuration to take into account the influence of WEc. Fig. 5B shows the current responses of WEc for several sizes Wc, for $G = 2$ and $W = 2$. Fig. 5C reports same data using logarithmic scales. For comparison, the concentration variation at the mid-gap distance was also plotted in absence of WEc (*i.e.*, when $W_c = 0$). As expected, when W_c increases in the range between 0 and G, the time delay decreases here between 4 to 1 approximately (Fig. 5C). Obviously, the upper value corresponds to the situation described previously for the 2WE configuration with same geometry (W, G). In this

hypothetical case, the size of WEc is so small that this electrode does not disturb the concentration gradients established between WEs. WEc then acts as a concentration probe with high spatial and temporal resolution at its location on the microchannel floor [55]. Conversely, the lower value close to unity is the limit reached when there is no longer any effect of the geometry (*W*, *W*c, *G*). It corresponds to the condition when diffusion becomes only controlled by the microchannel height. From a theoretical point of view, these limiting situations are easily predictable and assessable from Fig. 4. However, note that the simulations show a drastic influence of WEc on the delay (*see* Fig. 5C).

4.4. Experimental illustrations

The microdevice depicted in Fig. S1A was used to experimentally analyze the depletion performance achieved within a microchannel. The microdevice comprised two independent electrochemical cells of three parallel microband electrodes with the sequence WEs / WEc / WEs. The cells had different characteristic gap distances, either g = 130 or 230 µm. These distances were selected to experimentally demonstrate time delays of at least a few seconds. Other geometric parameters are indicated in Fig. S1B. Note that only one cell is used and connected during one experiment.

The first set of experiments were performed with $Fe(CN)_6^{4-}$ as the single redox species within the microchannel. In this case, the electrodes were biased at 0.4 V to oxidize $Fe(CN)_6^{4-}$ to $Fe(CN)_6^{3-}$. In order to test the 2WE configuration, only the side electrodes WEs were connected. Fig. 6A reports the current responses of WEs monitored in each cell. In the single mode, only one WEs is connected unlike in the dual mode where both are connected. As expected, each WEs displayed in each pair the same current variations due to the symmetry of the device. Also, depending on the depletion rate, the shorter the gap, the lower the current variations. These behaviors were confirmed by comparing the experimental responses with simulated data, thus showing very good agreement. Depletion is attained after approximately a few tens of seconds. Theoretically, the times required to reach the PLc regime were t = 35 s and t = 11 s for g = 230 µm and g = 130 µm respectively (*i.e.*, which corresponded in dimensionless values to τ = 53 and τ = 17 for G = 11.5 and G = 6.5 considering D = 6 10^{-6} cm^2 s^{-1}; *see* zone diagram in Fig.2D). To some extent, these results validated here the predictions established above for the 2WE configuration.

The microdevice was also tested in the 3WE configuration with the two modes ON and OFF previously described in the experimental section. In mode ON, all the three electrodes were biased simultaneously whereas in mode OFF, only WEc was polarized. All the WEc responses were plotted together in Fig. 6B. In mode OFF, the current decay was that of a single microband operating within a microchannel. Indeed, at long times and unlike in open solution, no pseudo-steady state is reached since the planar lateral diffusion predominates due to the confinement. As a result, the current decreases as a function of time and tends to zero. In mode ON, the current decreases much faster due the depletion of redox species produced by the side-electrodes WEs. As soon as the diffusion coupling takes place between all the electrodes, the current of WEc tends towards zero whereas those of WEs (which are identical in magnitude due to symmetry) still decay with time (as in Fig. 6A). This behavior confirms the strong decrease of concentration in the mid-gap of the electrochemical cell while planar lateral diffusion PLc still operates at both WEs. The same trend was observed for the two electrochemical cells. The decays in current were then compared in Fig. 6B-D with those simulated. A very good agreement was found between data validating the simulations performed under these conditions. However, to illustrate in both cases the influence of WEc on depletion rate, concentrations were also simulated at the mid-gap distance without the presence of WEc (*i.e.*, in a 2WE configuration with the same interelectrode distance g). As in Fig. 5C, the resulting variations were plotted in Figs. 6C-D using the dual scale ordinate. As expected, the experimental currents fall at times shorter than the simulated concentrations due to the operation of WEc. Indeed, under these conditions, the relatively large width of WEc do not allow the electrode to behave as a concentration probe without locally altering the concentration profiles by the development of its own diffusion layer. Time shifts Δt of 38 s and 13 s were obtained in Figs. 6C-D for g = 230 µm and g = 130 µm respectively (*i.e.*, $\Delta\tau$ = 57 and $\Delta\tau$ = 19 for G = 11.5 and G = 6.5). Note that these Δt values were estimated on the plots at half the current and concentration variations. Note also in Figs. 6C-D that the residual currents measured at long times deviate from simulated currents, firstly due to the lower accuracy of measurements at such a current intensity level (< nA) and secondly due to the influence of background currents. Graphically, from simulated currents, quantitative depletions are

expected beyond t = 30 s and t = 10 s for g = 230 µm and g = 130 µm respectively (*i.e.*, beyond τ = 45 and τ = 15 for G = 11.5 and G = 6.5).

In the second set of experiments, the microdevice was used to illustrate the depletion effect with a mixture of two redox species, a mixture of NO_2^- and H_2O_2 with one being the species to detect and the other the interferent. In this case, H_2O_2 with the lowest oxidation potential is the interfering species with respect to the electrochemical detection of NO_2^-. In this context, the application was therefore to selectively detect NO_2^- at WEc while fully depleting H_2O_2 by the operation of WEs. Figs. 7A-B report cyclic voltammograms recorded at WEc, in modes ON and OFF, either in a H_2O_2 solution (Fig. 7A) or in an equimolar mixture (NO_2^- + H_2O_2) (Fig. 7B). Under these conditions, the side electrodes WEs were biased at 0.5 V and the potential scan at WEc was set to 0.01 $V.s^{-1}$. This latter was low enough to allow the diffusion coupling between the electrodes during each cycle. Fig. 7A shows that in mode OFF the irreversible H_2O_2 oxidation wave was around 0.2 V and that it was totally suppressed in mode ON. Conversely, Fig. 7B shows that the NO_2^- irreversible oxidation wave was identified at 0.75 V and observed in both modes. Therefore, these results confirmed the extreme selectivity achieved during NO_2^- detection by applying the right potentials to each electrode. In order to perform quantitative evaluations of the depletion rate, chronoamperometric experiments were then performed by analyzing the responses of WEc separately in the mixture (NO_2^- + H_2O_2) and in a NO_2^- solution of same concentration (Figs. 7C-D). WEc was biased at 0.85 V while the side electrodes WEs were biased at 0.5 V (in mode ON). Fig. 7C highlights the establishment of H_2O_2 depletion as a function of time. The curves with the mixture in mode ON and the curve with NO_2^- solution were almost superimposed, in agreement with the simulated response assuming a two-electron transfer for NO_2^- oxidation (black dashed line). The transition in current can best be analyzed in Fig. 7D by plotting the same responses using logarithmic scales. As in Fig. 6D with the same geometry (i.e., g = 130 µm), a time delay of about 4 s (*i.e.*, τ = 15 with D = 1.5 10^{-5} cm^2s^{-1}) could be clearly estimated in mode ON. In particular, the key feature is that the current response of WEc tended within the experimental uncertainties towards that monitored in the separate NO_2^- solution, thus demonstrating the total depletion of H_2O_2 and selective detection of NO_2^-.

The two examples given above illustrate the concept of depletion by two side electrodes and the simulations led to accurate predictions with regard to the experimental conditions used. Evaluations based on a 3WE configuration cannot be generalized to any experimental conditions due to multiple possible geometries. Nevertheless, boundary limits for time delays can be easily assessed from predictions based on the 2WE configuration given in Figs 3-4. Note that using a third electrode to probe concentrations or to detect species with high selectivity is only part of the applications deriving potentially from the concept. Indeed, the 2WE configuration involves broader experimental conditions for potential applications where depletion of redox species is required between two electrodes.

5. Conclusion

This study took advantage of the spatial constraints exerted in the vicinity of paired microband electrodes to assess the depletion of electroactive species in absence of flux. Depending on the geometry and configuration of the electrochemical cell, an electroactive-species depleted microenvironment in the interelectrode space can be generated at a sufficiently short polarization time with very high efficiency. Minimal cell configurations with two or three working electrodes were considered to analyze mass transport regimes as a function of time. In particular, numerical simulations were performed to reach the situation of interest when diffusion coupling and lateral diffusion in the microchannel become predominant. A wide range of conditions was defined by establishing a zone diagram and identifying boundary conditions. Depletion rates were evaluated from current variations, which ultimately allow the expected performance to be controlled from experimental current responses. These results were successfully validated experimentally in the 2WE configuration for bulk electrolysis and in the 3WE configuration for selective detection with total elimination of interfering species. All of these assessments apply to sensing applications, especially in microfluidics where stopped-flow mode is expected. Moreover, these conditions can be easily extrapolated to the cases of regular microelectrode arrays inside microchannels. Indeed, the influence of confinement here is only dictated by the geometry of the interelectrode space (*i.e.*, based on the minimal configurations 2WE and 3WE) and not by the number of electrodes.

Acknowledgements

This work was supported in parts by CNRS UMR 8640, ENS (Ecole normale superieure), PSL University and Sorbonne Université.

References

[1] D. Li, C. Batchelor-McAuley, L. Chen, R.G. Compton, Band Electrodes in Sensing Applications: Response Characteristics and Band Fabrication Methods, ACS Sens., 4 (2019) 2250-2266.

[2] N. Karimian, P. Ugo, Recent advances in sensing and biosensing with arrays of nanoelectrodes, Curr Opin Electrochem, 16 (2019) 106-116.

[3] Y. Liu, X. Li, J. Chen, C. Yuan, Micro/Nano Electrode Array Sensors: Advances in Fabrication and Emerging Applications in Bioanalysis, Front. Chem., 8 (2020) 573865.

[4] E. Kosri, F. Ibrahim, A. Thiha, M. Madou, Micro and Nano Interdigitated Electrode Array (IDEA)-Based MEMS/NEMS as Electrochemical Transducers: A Review, Nanomaterials-Basel, 12 (2022).

[5] Y. Yu, H.Y.Y. Nyein, W. Gao, A. Javey, Flexible Electrochemical Bioelectronics: The Rise of In Situ Bioanalysis, Adv. Mater., 32 (2020) e1902083.

[6] P. Tomcik, Microelectrode arrays with overlapped diffusion layers as electroanalytical detectors: theory and basic applications, Sens., 13 (2013) 13659-13684.

[7] R.M. Wightman, Microvoltammetric electrodes, Anal. Chem., 53 (1981) 1125A-1134A.

[8] K. Stulik, C. Amatore, K. Holub, V. Marecek, W. Kutner, Microelectrodes. Definitions, characterization, and applications (Technical Report), Pure Appl Chem, 72 (2000) 1483-1492.

[9] J. Heinze, Ultramicroelectrodes in Electrochemistry, Angew. Chem. Int. Ed., 32 (1993) 1268-1288.

[10] J.C. Jaton, H. Huser, Y. Blatt, I. Pecht, Circular dichroism and fluorescence studies of homogeneous antibodies to type III pneumococcal polysaccharide, Biochemistry, 14 (1975) 5308-5311.

[11] E.O. Barnes, G.E. Lewis, S.E. Dale, F. Marken, R.G. Compton, Generator-collector double electrode systems: a review, Analyst, 137 (2012) 1068-1081.

[12] F. Zhu, B.W. Mao, J.W. Yan, Double electrode systems with microelectrode arrays for electrochemical measurements, Rev Anal Chem, 34 (2015) 87-101.

[13] U. Wollenberger, M. Paeschke, R. Hintsche, Interdigitated Array Microelectrodes for the Determination of Enzyme-Activities, Analyst, 119 (1994) 1245-1249.

[14] T.A. Postlethwaite, J.E. Hutchison, R. Murray, B. Fosset, C. Amatore, Interdigitated array electrode as an alternative to the rotated ring-disk electrode for determination of the reaction products of dioxygen reduction, Anal. Chem., 68 (1996) 2951-2958.

[15] M. Hu, I. Fritsch, Redox cycling behavior of individual and binary mixtures of catecholamines at gold microband electrode arrays, Anal. Chem., 87 (2015) 2029-2032.

[16] D. Menshykau, M. Cortina-Puig, F.J. del Campo, F.X. Munoz, R.G. Compton, Plane-recessed disk electrodes and their arrays in transient generator-collector mode: The measurement of the rate of the chemical reaction of electrochemically generated species, J. Electroanal. Chem., 648 (2010) 28-35.

[17] J.E. Bartelt, M.R. Deakin, C. Amatore, R.M. Wightman, Construction and Use of Paired and Triple Band Microelectrodes in Solutions of Low Ionic-Strength, Anal. Chem., 60 (1988) 2167-2169.

[18] B. Fosset, C. Amatore, J. Bartelt, R.M. Wightman, Theory and Experiment for the Collector-Generator Triple-Band Electrode, Anal. Chem., 63 (1991) 1403-1408.

[19] B. Fosset, C.A. Amatore, J.E. Bartelt, A.C. Michael, R.M. Wightman, Use of Conformal-Maps to Model the Voltammetric Response of Collector Generator Double-Band Electrodes, Anal. Chem., 63 (1991) 306-314.

[20] C. Amatore, N. Da Mota, C. Lemmer, C. Pebay, C. Sella, L. Thouin, Theory and experiments of transport at channel microband electrodes under laminar flows. 2. Electrochemical regimes at double microband assemblies under steady state, Anal. Chem., 80 (2008) 9483-9490.

[21] K. Aoki, K. Tokuda, H. Matsuda, Hydrodynamic voltammetry at channel electrodes: Part II. Theory of first-order kinetic collection efficiencies, J. Electroanal. Chem., 79 (1977) 49-78.

[22] A.C. Fisher, R.G. Compton, Double-Channel Electrodes - Homogeneous Kinetics and Collection Efficiency Measurements, J. Appl. Electrochem., 21 (1991) 208-212.

[23] P.M. Lewis, L.B. Sheridan, R.E. Gawley, I. Fritsch, Signal amplification in a microchannel from redox cycling with varied electroactive configurations of an individually addressable microband electrode array, Anal. Chem., 82 (2010) 1659-1668.

[24] T.R.L.C. Paixao, R.C. Matos, M. Bertotti, Design and characterisation of a thin-layered dual-band electrochemical cell, Electrochim. Acta, 48 (2003) 691-698.

[25] E.D. Goluch, B. Wolfrum, P.S. Singh, M.A. Zevenbergen, S.G. Lemay, Redox cycling in nanofluidic channels using interdigitated electrodes, Anal. Bioanal. Chem., 394 (2009) 447-456.

[26] B. Wolfrum, E. Katelhon, A. Yakushenko, K.J. Krause, N. Adly, M. Huske, P. Rinklin, Nanoscale Electrochemical Sensor Arrays: Redox Cycling Amplification in Dual-Electrode Systems, Acc. Chem. Res., 49 (2016) 2031-2040.

[27] O. Niwa, M. Morita, H. Tabei, Fabrication and Characteristics of Vertically Separated Interdigitated Array Electrodes, J. Electroanal. Chem., 267 (1989) 291-297.

[28] D. Menshykau, A.M. O'Mahony, F.J. del Campo, F.X. Munoz, R.G. Compton, Microarrays of ring-recessed disk electrodes in transient generator-collector mode: theory and experiment, Anal. Chem., 81 (2009) 9372-9382.

[29] O. Niwa, M. Morita, H. Tabei, Electrochemical-Behavior of Reversible Redox Species at Interdigitated Array Electrodes with Different Geometries - Consideration of Redox Cycling and Collection Efficiency, Anal. Chem., 62 (1990) 447-452.

[30] K. Aoki, Theory of Stationary Current-Potential Curves at lnterdigitated Microarray Electrodes for Quasi-Reversible and Totally Irreversible Electrode Reactions, Electroanalysis, 2 (1990) 229-233.

[31] J.I. Heo, Y. Lim, H. Shin, The effect of channel height and electrode aspect ratio on redox cycling at carbon interdigitated array nanoelectrodes confined in a microchannel, Analyst, 138 (2013) 6404-6411.

[32] A.J. Bard, M.V. Mirkin, P.R. Unwin, D.O. Wipf, Scanning electrochemical microscopy. 12. Theory and experiment of the feedback mode wih finite heterogeneous electron-transfer kinetics and arbitrary substrate size, J. Phys. Chem., 96 (1992) 1861-1868.

[33] I. Streeter, N. Fietkau, J. Del Campo, R. Mas, F.X. Munoz, R.G. Compton, Voltammetry at regular microband electrode arrays: Theory and experiment, J. Phys. Chem. C, 111 (2007) 12058-12066.

[34] F. Zhu, J.W. Yan, M. Lu, Y.L. Zhou, Y. Yang, B.W. Mao, A strategy for selective detection based on interferent depleting and redox cycling using the plane-recessed microdisk array electrodes, Electrochim. Acta, 56 (2011) 8101-8107.

[35] A. Oleinick, F. Zhu, J. Yan, B. Mao, I. Svir, C. Amatore, Theoretical investigation of generator-collector microwell arrays for improving electroanalytical selectivity: application to selective dopamine detection in the presence of ascorbic acid, Chemphyschem, 14 (2013) 1887-1898.

[36] S.W. Pang, J.W. Yan, F. Zhu, D.W. He, B.W. Mao, A. Oleinick, I. Svir, C. Amatore, A new strategy for eliminating interference from EC' mechanism during analytical measurements based on plane-band-recessed microdisk array electrodes, Electrochem. Commun., 38 (2014) 61-64.

[37] D.A. Finkelstein, Sensor Selectivity Enhancement via Electrochemical Shielding in a Recessed Microelectrode Array: The Gatekeeper Geometry, Acs Sens., 1 (2016) 1217-1221.

[38] D. He, J. Yan, F. Zhu, Y. Zhou, B. Mao, A. Oleinick, I. Svir, C. Amatore, Enhancing the Bipolar Redox Cycling Efficiency of Plane-Recessed Microelectrode Arrays by Adding a Chemically Irreversible Interferent, Anal. Chem., 88 (2016) 8535-8541.

[39] T. Horiuchi, O. Niwa, M. Morita, H. Tabei, Limiting Current Enhancement by Self-Induced Redox Cycling on a Micro-Macro Twin Electrode, J. Electrochem. Soc., 138 (1991) 3549-3553.

[40] H. Tabei, T. Horiuchi, O. Niwa, M. Morita, Highly Sensitive Detection of Reversible Species by Self-Induced Redox Cycling, J. Electroanal. Chem., 326 (1992) 339-343.

[41] J. Kwak, A.J. Bard, Scanning Electrochemical Microscopy - Theory of the Feedback Mode, Anal. Chem., 61 (1989) 1221-1227.

[42] P.C. Nien, P.Y. Chen, C.Y. Hsu, K.C. Ho, On-chip glucose biosensor based on enzyme entrapment with pre-reaction to lower interference in a flow injection system, Sens. Actuators B Chem., 157 (2011) 64-71.

[43] T. Watanabe, S. Shibano, H. Maeda, A. Sugitani, M. Katayama, Y. Matsumoto, Y. Einaga, Fabrication of a Microfluidic Device with Boron-doped Diamond Electrodes for Electrochemical Analysis, Electrochim. Acta, 197 (2016) 159-166.

[44] R. Oliveira, C. Sella, C. Souprayen, E. Ait-Yahiatene, C. Slim, S. Griveau, L. Thouin, F. Bedioui, Development of a flow microsensor for selective detection of nitric oxide in the presence of hydrogen peroxide, Electrochim. Acta, 286 (2018) 365-373.

[45] J. Gouyon, F. d'Orlye, C. Simon, S. Griveau, C. Sella, L. Thouin, F. Bedioui, A. Varenne, Reversible microfluidics device for precious metal electrodeposition and depletion yield studies, Electrochim. Acta, 352 (2020) 136474.

[46] C. Amatore, N. Da Mota, C. Sella, L. Thouin, Theory and experiments of transport at channel microband electrodes under laminar flows. 1. Steady-state regimes at a single electrode, Anal. Chem., 79 (2007) 8502-8510.

[47] J.C. Jaton, H. Huser, D.G. Braun, D. Givol, I. Pecht, J. Schlessinger, Conformational changes induced in a homogeneous anti-type III pneumococcal antibody by oligosaccharides of increasing size, Biochemistry, 14 (1975) 5312-5315.

[48] O. Scialdone, C. Guarisco, A. Galia, G. Filardo, G. Silvestri, C. Amatore, C. Sella, L. Thouin, Anodic abatement of organic pollutants in water in micro reactors, J. Electroanal. Chem., 638 (2010) 293-296.

[49] R. Oliveira, F. Bento, C. Sella, L. Thouin, C. Amatore, Direct electroanalytical method for alternative assessment of global antioxidant capacity using microchannel electrodes, Anal. Chem., 85 (2013) 9057-9063.

[50] W. Bellagha-Chenchah, C. Sella, L. Thouin, Understanding Mass Transport at Channel Microband Electrodes: Influence of Confined Space under Stagnant Conditions, Electrochim. Acta, 202 (2016) 122-130.

[51] H. Ikeuchi, M. Kanakubo, Determination of diffusion coefficients of the electrode reaction products by the double potential step chronoamperometry at small disk electrodes, J. Electroanal. Chem., 493 (2000) 93-99.

[52] Y. Li, C. Sella, F. Lemaître, M. Guille Collignon, L. Thouin, C. Amatore, Highly Sensitive Platinum-Black Coated Platinum Electrodes for Electrochemical Detection of Hydrogen Peroxide and Nitrite in Microchannel, Electroanalysis, 25 (2013) 895-902.

[53] A. Szabo, D.K. Cope, D.E. Tallman, P.M. Kovach, R.M. Wightman, Chronoamperometric Current at Hemicylinder and Band Microelectrodes - Theory and Experiment, J. Electroanal. Chem., 217 (1987) 417-423.

[54] I.A. Arkoub, C. Amatore, C. Sella, L. Thouin, J.S. Warkocz, Diffusion at double microband electrodes operated within a thin film coating. Theory and experimental illustration, J. Phys. Chem. B, 105 (2001) 8694-8703.

[55] C. Amatore, C. Lemmer, P. Perrodin, C. Sella, L. Thouin, Theory and experiments of microelectrodes performing as concentration probes within microfluidic channels with high temporal resolution, Electrochem. Commun., 13 (2011) 1459-1461.

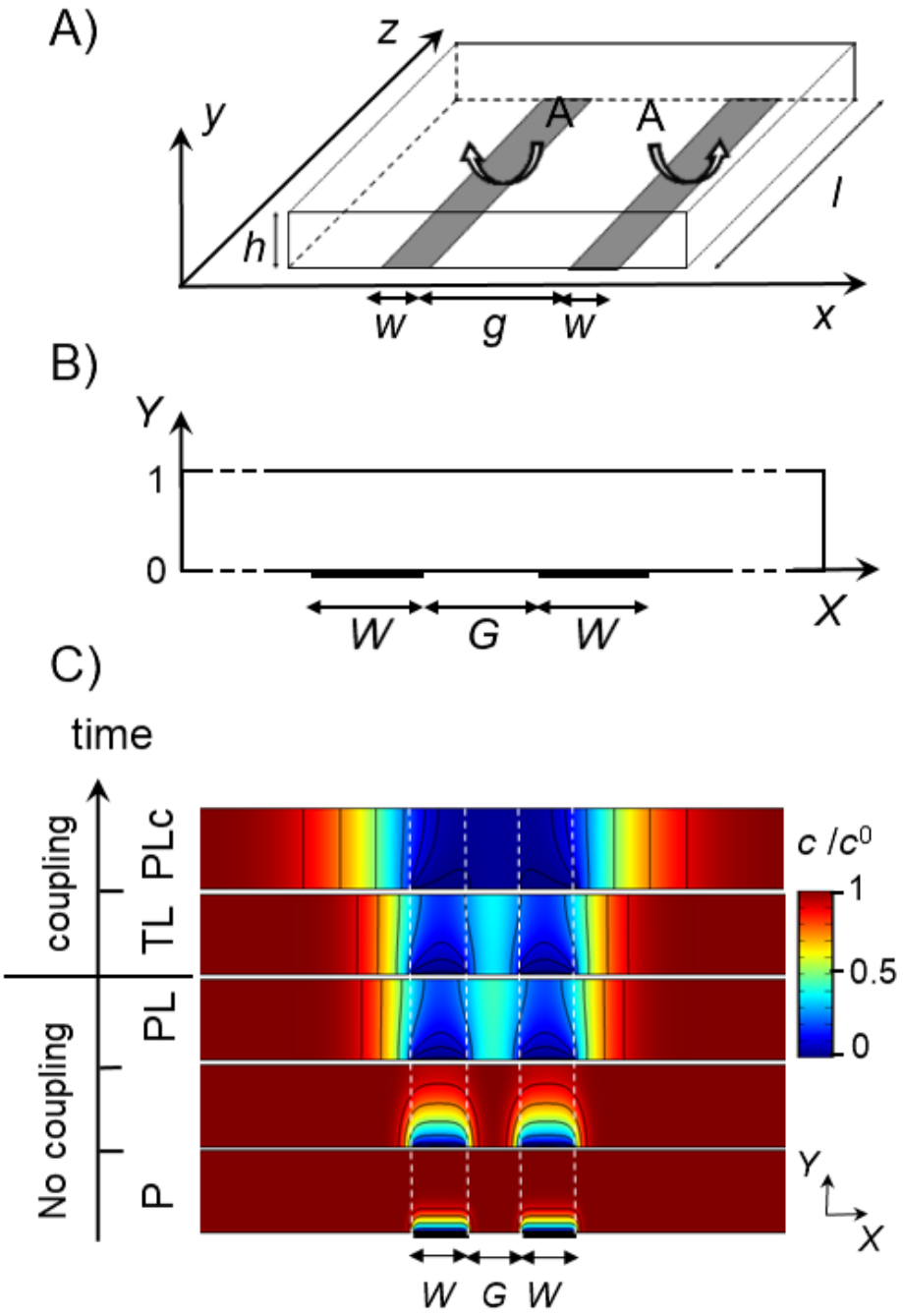

Fig. 1: Two-working-electrode (2WE) configuration in a microchannel. A) 3D scheme of the device in real space (x,y,z) with microband widths w, gap distance g, microchannel height h and microchannel length l. B) 2D scheme of the device in the dimensionless space (X,Y) used for numerical simulations. (C) Concentration profiles simulated for $W = 2$, $G = 2$ and times $\tau = 0.01$, 0.1, 1.1, 1.25 and 4. The black curves represent seven isoconcentration lines for $c/c^0 = 0.90$, 0.75, 0.50, 0.25, 0.1, 0.05, 0.01. The Y-scale is expanded 3 times compared to the X-scale.

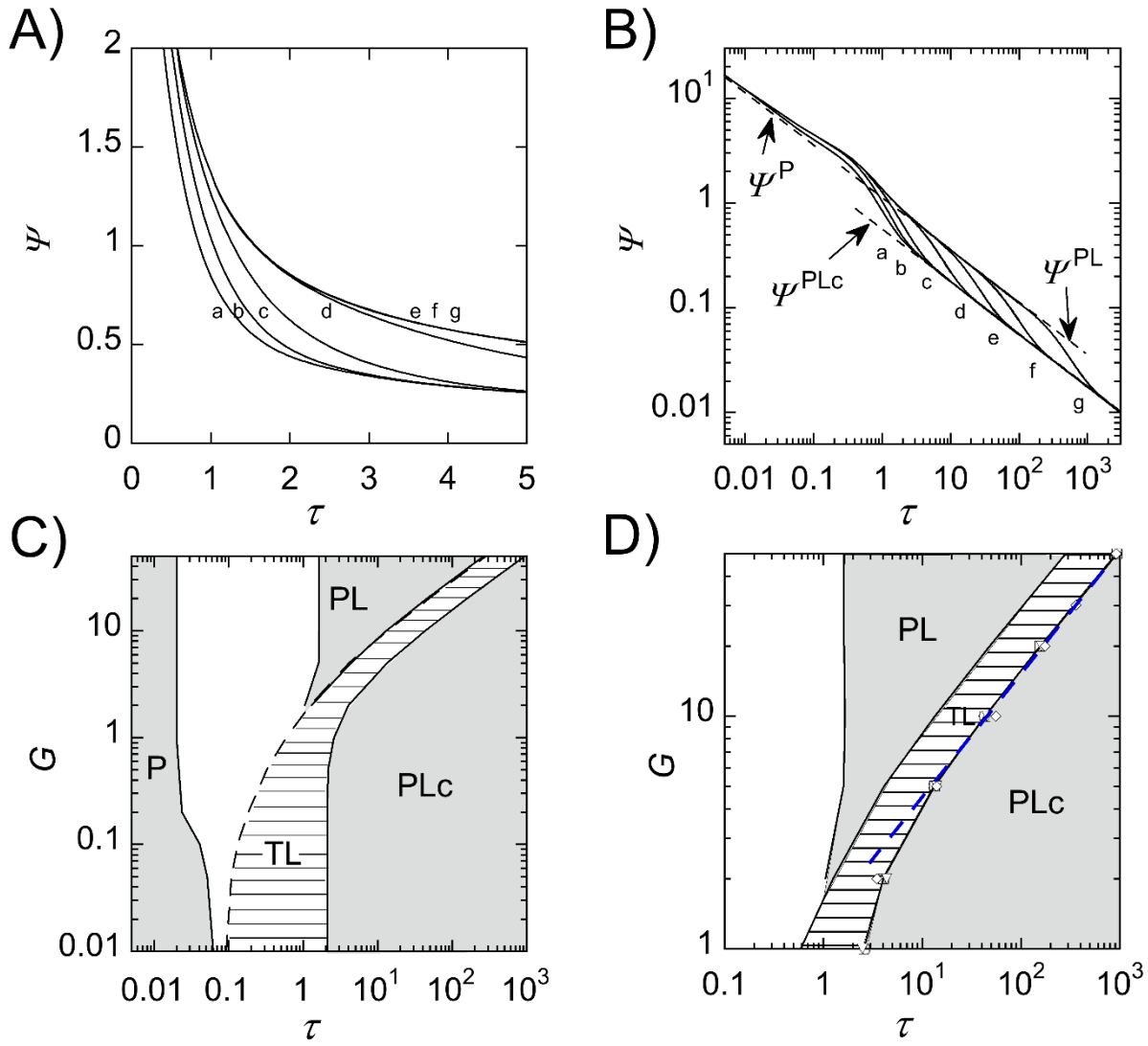

Fig. 2: (A) Dimensionless currents Ψ as a function of time τ in chronoamperometry at paired microband electrodes with $W = 2$ and $G = 0.1$ (a),1 (b), 2 (c), 5 (d), 10(e), 20 (f), 50 (g). B) Logarithmic plot of A; the three dashed lines correspond to limiting regimes: Ψ^{P} Eq. (4) for planar diffusion, Ψ^{PL} Eq. (5) for lateral diffusion and Ψ^{PLc} Eq. (6) for planar lateral diffusion. (C) Zone diagram (G, τ) established for paired microband electrodes with $W = 2$ showing prevalence areas of regimes P, PL, PLc and TL. The dashed line delineates the boundary between TL and PLc regimes controlled by the diffusion coupling between the electrodes. (D) Part of the (G, τ) diagram (*i.e.*, $G \geq 1$) with the boundary TL/PLc determined for several electrode widths: $W = 0.1$ (◊), 1 (Δ), 2 (□) and 5 (○). For $G > 4$, the transition TL/PLc can be approximated by $G = 1.58\ \tau^{0.5}$ (blue dashed line, Eq. (8)).

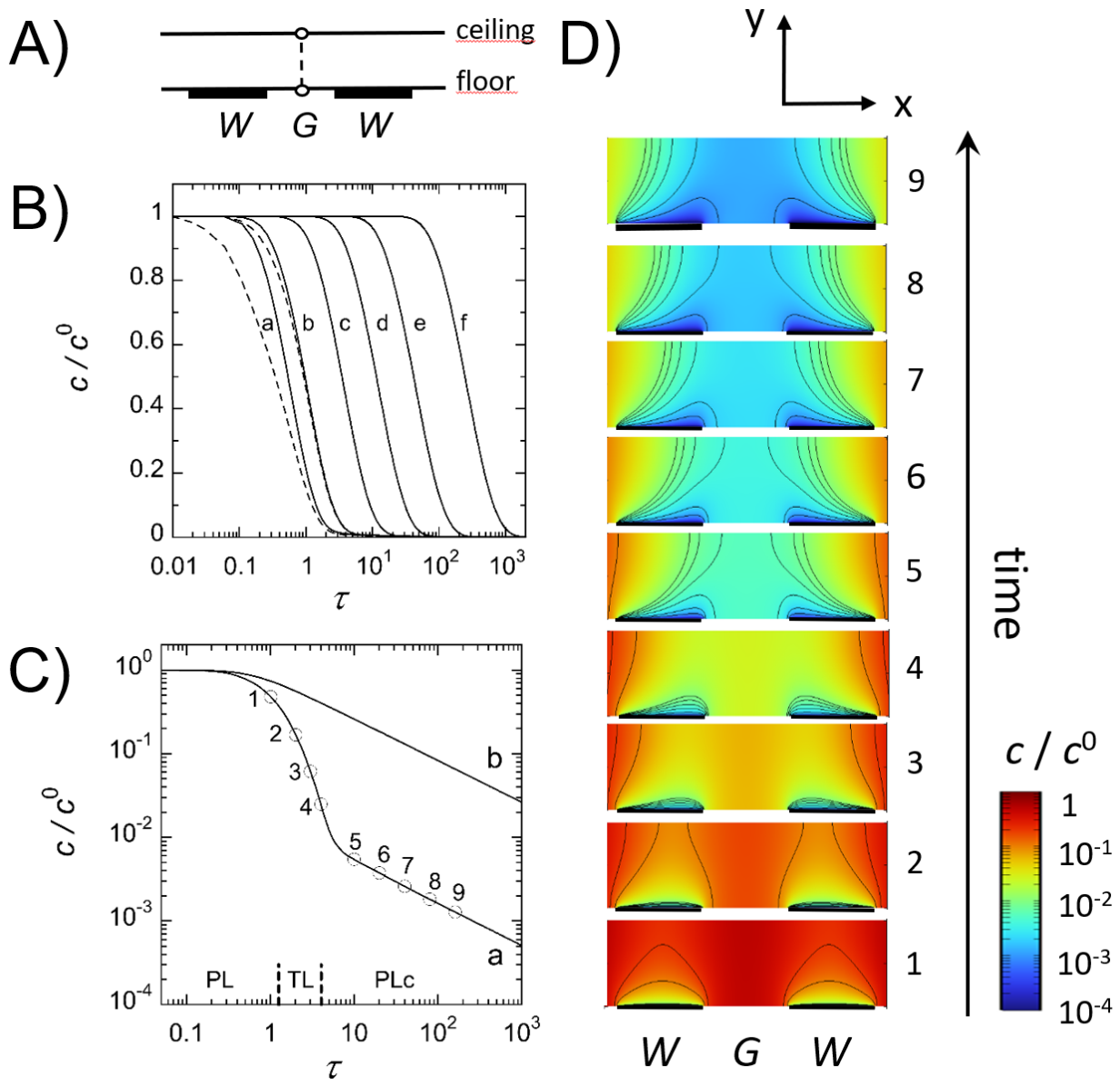

Fig. 3: A) Location of the two dimensionless concentrations c/c^0 (circles) monitored at the mid-distance between the electrodes, on the floor and ceiling of the microchannel. B) Concentrations simulated on the ceiling (dashed line) and floor (solid line) as a function of time for $W = 2$ and $G = 1$ (a), 2 (b), 5 (c), 10 (d), 20 (e), and 50 (f); In (c-f), the solid and dashed lines are superimposed. C) Logarithmic representation of concentrations simulated at the floor for $G = 2$ (a) and $G > 100$ (b). D) Concentration profiles corresponding to different times in (C) for $G = 2$; the Y-scale is expanded twice.

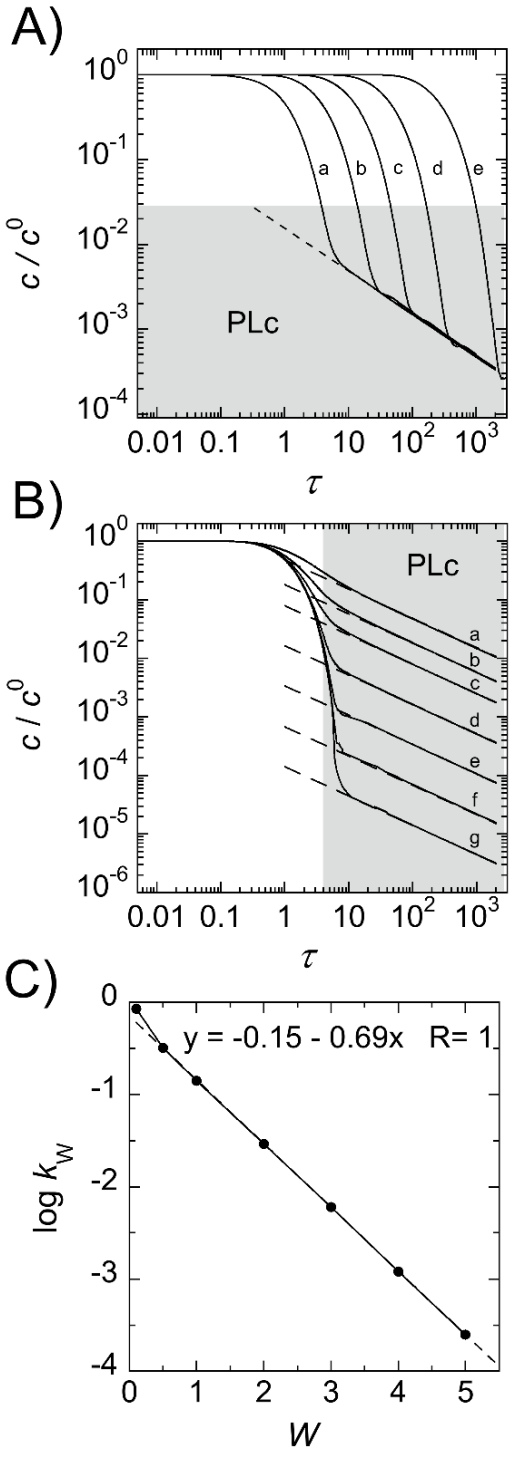

Fig. 4: Simulated concentrations at the mid-distance between the electrodes. A) Variations of concentration versus time for $G = 2$ (a), 5 (b), 10 (c), 20 (d), 50 (e) and $W = 2$; c. B) Variations of concentration versus time for $W = 0{,}1$ (a), 0,5 (b), 1 (c), 2 (d), 3 (e), 4 (f), 5 (g), and $G = 2$. C) Variation of k_w as a function of W (Eq. (10)).

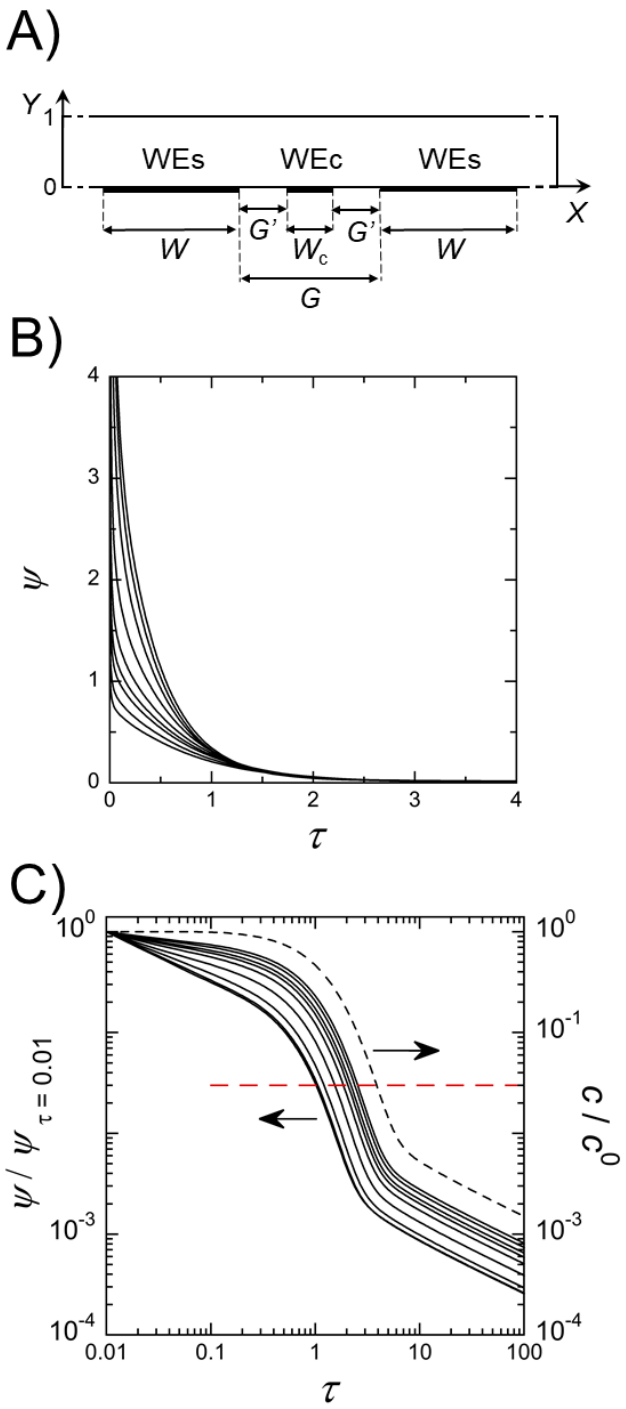

Fig. 5: Three-working-electrode (3WE) configuration in a microchannel. A) 2D scheme of the device in the dimensionless space (X,Y) used for numerical simulations. B) Simulated WEc currents for W_c = 0.025 to 1.9 (series of curves from right to left. C) Logarithmic plots of data in B; Comparison with the simulated mid-gap concentrations (dashed line) in the 2WE configuration. In (A-C), W = G = 2.

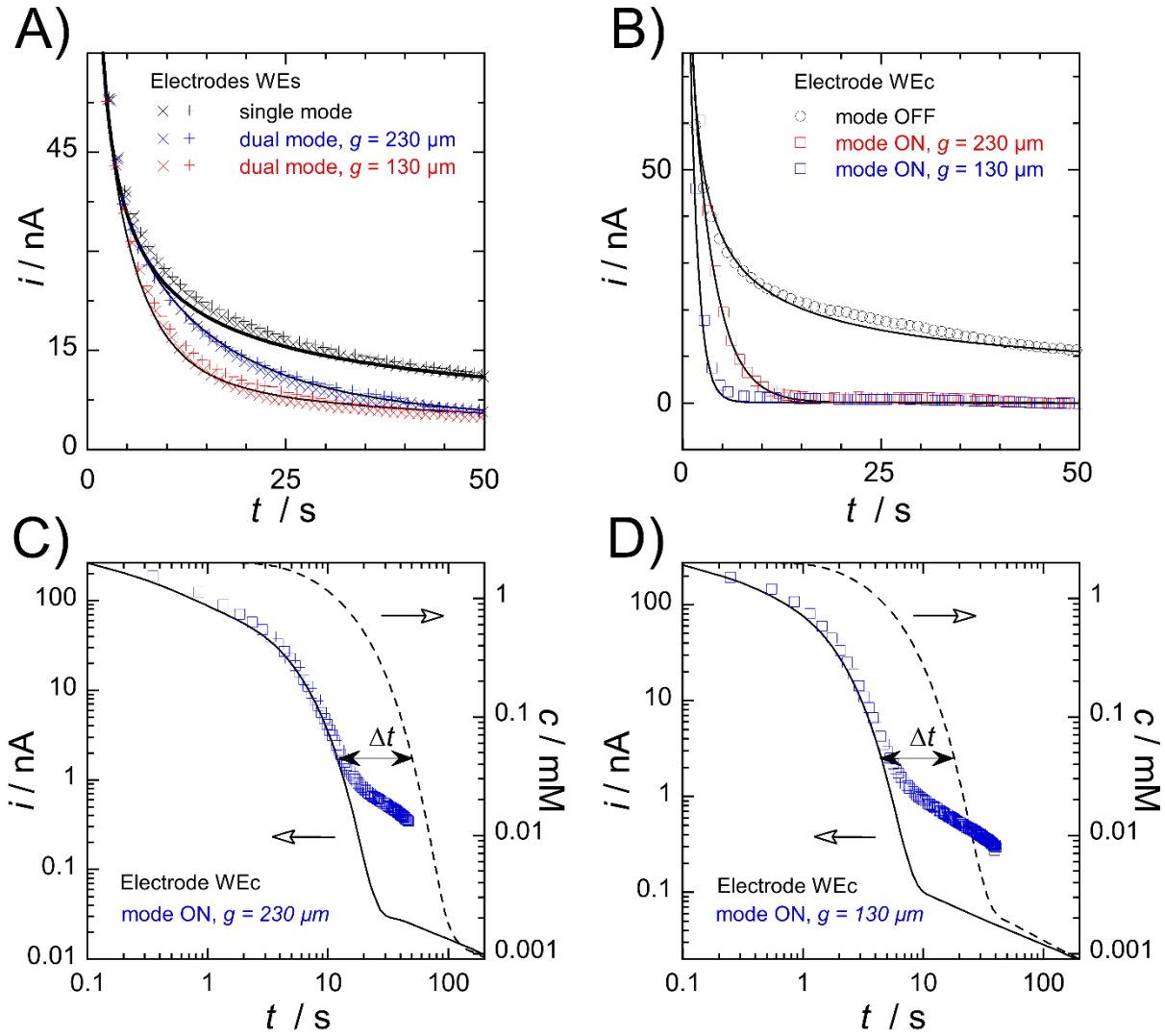

Fig. 6: Experimental (symbols) and simulated (lines) current responses in chronoamperometry. A) 2WE configuration with WEs currents in single and dual modes. B) 3WE configuration with WEc currents in mode OFF and ON. C) Comparison between WEc currents (3WE configuration, mode ON) and mid-gap simulated concentrations (2WE configuration) for g = 230 µm. D) Same as in C but for g = 130 µm. In A-D) Microchannel dimensions h = 20 µm and l = 800 µm; 2 mM $Fe(CN)_6^{4-}$ in 0.01 M PBS; electrodes biased at 0.4V /Ag/AgCl.

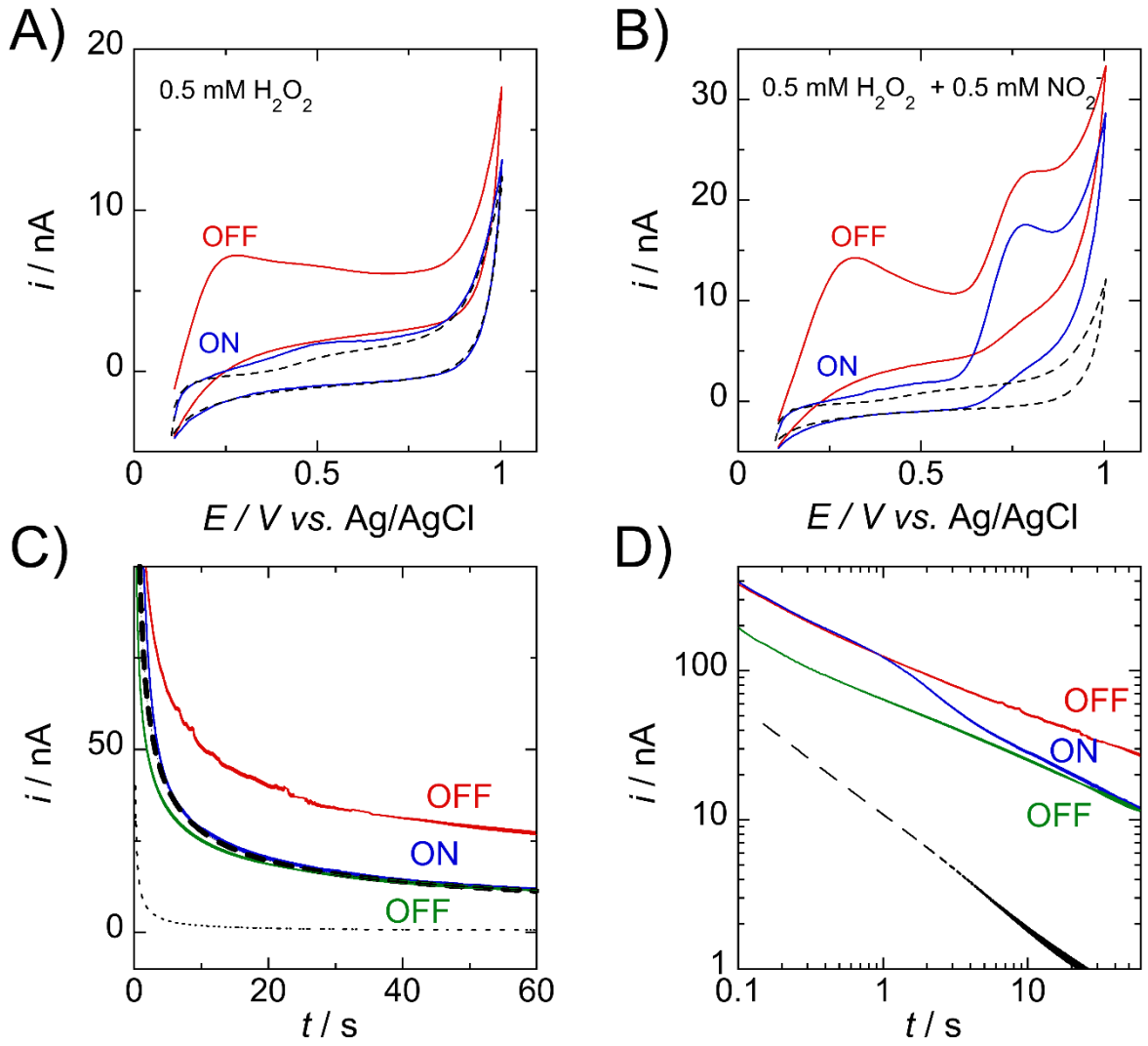

Fig. 7: Experimental currents recorded at WEc electrode for g = 130 µm in modes ON and OFF in 3WE configuration. A-B) Cyclic voltammetry in 0.5 mM H_2O_2 (A) and in a mixture 0.5 mM H_2O_2 + 0.5 mM NO_2^- (B) at 0.01 $V.s^{-1}$ scan rate. C) Chronoamperometry at 0.85 V/Ag/AgCl in a mixture 1 mM H_2O_2 + 1 mM NO_2^- (red and blue), and in 0.5 mM NO_2^- (green); simulated current response (thick black dashed line). D) Logarithmic plots of data in C. In (A-D) WEs are biased at 0.5 V/ Ref while WEc is biased at 0.85 V / Ref; the current responses in PBS are plotted in dashed lines.

Graphical abstract